An Embedded Boundary Method for the Modeling of Unsteady Combustion in an Industrial Gas-Fired Furnace *

Richard B. Pember, Ann S. Almgren, William Y. Crutchfield,
Louis H. Howell, John B. Bell, Phillip Colella, and Vincent E. Beckner
Lawrence Livermore National Laboratory,
P.O. Box 808, L-316,
Livermore, CA 94550
e-mail: pember@llnl.gov

Abstract

A new methodology for the modeling of unsteady, nonpremixed, axisymmetric reacting flow in industrial furnaces is presented. The method is an extension of previous work by the authors to complex geometries, multistep kinetics mechanisms, and realistic properties, especially thermochemical data. The walls of the furnace are represented as an embedded boundary in a uniform, rectangular grid. The grid then consists of uniform rectangular cells except at the furnace wall where irregular (mixed) cells may be present. We use finite volume differencing techniques for the convective, viscous, and radiative heat transport terms in the mixed cells, while a finite element-based technique is used to solve the elliptic equation arising from the low-Mach number formulation. Results from the simulation of an experimental natural gas-fired furnace are shown.

1 Introduction

The ability to model transient effects in furnaces is becoming increasingly important. The problem of ensuring the safe performance of an industrial furnace, for example, is more difficult during the startup or shutdown phases of operation than during normal operating conditions. Further, the peak formation of pollutants is much more dependent on transient behavior, in particular, on peak temperatures, than on average operating conditions.

We present in this paper a new methodology for the modeling of unsteady, nonpremixed reacting flow in industrial furnaces. The method is an extension of previous work by the authors [25] to complex geometries, multistep kinetics mechanisms, and realistic properties, especially thermochemical data. Results from the simulation of an experimental natural gas-fired furnace are shown.

The methodology rests on the assumption that combustion in an industrial furnace is a low-Mach number flow. In such flows, the time scale of the acoustics is much smaller than the convective time scale, and acoustic effects are weak relative to advective effects. Under this assumption, then, detailed acoustic effects can be removed from the governing system of equations. The low-Mach number formulation thus enables the solution of the equations with a projection methodology that uses explicit higher-order upwind differencing of the convective terms with a time step restricted solely by an advective Courant-Friedrichs-Lewy (CFL) condition.

The algorithm in this paper uses a second-order projection method for unsteady, low-Mach number reacting flow [20] which accounts for species diffusion, convective and radiative heat transfer, viscous transport, turbulence, and chemical kinetics. The projection method for low-Mach number reacting flow is an extension of a higher-order projection method for incompressible flow [5] to the equations of low-Mach number reacting flow [27, 24]. Our particular method is based on an approximate projection formulation [3]. The method is implemented in this paper for axisymmetric flows with swirl, although cylindrical symmetry is not a limitation. A $k - \epsilon$ model is used for turbulent transport[16]. Chemical kinetics is modeled using a a two-step scheme for natural gas combustion [30] coupled with a simplified turbulent kinetics model [6, 23]. Radiative transport is modeled using the discrete ordinates method [9, 12, 22]. Viscosity and thermal conductivity are modeled with simple polynomial correlations [17] while GRI-Mech thermochemical data [13] is used to compute enthalpies, heat capacities, and heats of formation. The equation of state is the perfect gas law.

The wall of the furnace is represented as a boundary embedded in a uniform, rectangular grid. Hence, the grid consists of uniform rectangular cells except at the fluid-furnace wall interface where irregular (mixed) cells may be present (Figure 1). Methods using this approach are called Cartesian grid methods or embedded boundary methods. In our particular approach, we use finite volume differencing techniques for the convective, viscous, and radiative heat transport terms in the mixed cells, as in [2, 26], while a finite element-based technique [2] is used to solve the elliptic equation arising from the low-Mach number formulation. The explicit convective differencing technique used in the mixed cells imposes no additional time step restrictions even though the mixed cells may be arbitrarily small. Embedded boundary methods are a useful alternative to body-fitted structured or unstructured grid methods; see [26] for further discussion.

There are a number of techniques for simulating reacting flow based on SIMPLE [8] and its extensions [14, 18]. Our method is qualitatively similar to SIMPLE in that SIMPLE also uses a sequential formulation with velocity-pressure corrections based on a projection methodology [10, 15]. A projection method for low-Mach number combustion is also presented in [11].

In §2 the model for low-Mach number flow is reviewed. The governing equations, the numerical algorithm, and numerical results are presented in §3, §4, and §5, respectively.

2

2 Model for Low-Mach Number Combustion

The system of equations for reacting flow considered here is based on a model for low-Mach number combustion[27, 24], which we now briefly review.

For flow in a spatially open domain the underlying assumption in the low-Mach number model is that M is sufficiently small ($M < .3$) so that the pressure p can be written as the sum of a temporally and spatially constant part p_{amb} and a dynamic part π,

$$p(r, z, t) = p_{amb} + \pi(r, z, t), \tag{2.1}$$

where $\pi/p_{amb} = O\left(M^2\right)$. All thermodynamic quantities are considered to be independent of π. The perfect gas law for a multi-component gas in a flow satisfying the low-Mach number assumption is then

$$\rho = p_{amb}/\left(T R_{mix}\right) = p_{amb}/\left(T\mathcal{R}/mw_{mix}\right) = p_{amb}/\left(T\mathcal{R}\sum_l \left(m_l/mw_l\right)\right), \tag{2.2}$$

where $\mathcal{R}$ is the universal gas constant, and m_l and mw_l are the mass fraction and the molecular weight of species l. Differentiating (2.2) with respect to time and using continuity, the following constraint on the divergence of the velocity is obtained:

$$\nabla \cdot U = \frac{1}{T}\frac{DT}{Dt} + mw_{mix}\sum_l \frac{1}{mw_l}\frac{Dm_l}{Dt}. \tag{2.3}$$

Expressions similar to (2.3) can be obtained if the equation of state is not the perfect gas law.

Note: In this paper we use the symbol U to refer to $(u, v)^T$ except in the context of the deformation gradient $\partial U_i/\partial x_j$, in which case U refers to $(u, v, w)^T$.

3 Governing Equations

The system of governing differential equations consists of the divergence constraint (2.3) and the following evolution equations for density, velocity, enthalpy, temperature, species concentrations, and turbulent kinetic energy and dissipation rate:

$$\frac{\partial \rho}{\partial t} + \nabla \cdot (\rho U) = 0. \tag{3.1}$$

$$\begin{pmatrix} \rho\dfrac{Du}{Dt} & -\dfrac{w^2}{r} \\[2mm] \rho\dfrac{Dv}{Dt} & \\[2mm] \dfrac{\partial\rho w}{\partial t} + \nabla \cdot (\rho U w) & +\dfrac{uw}{r} \end{pmatrix} = -\nabla\pi + \nabla \cdot \tau \tag{3.2}$$

$$\frac{\partial\rho h}{\partial t} + \nabla \cdot \rho U h = \nabla \cdot (\lambda + \lambda_t)\nabla T - \nabla \cdot q_{rad} + \nabla \cdot \sum_l \rho h_l(T)(D + D_t)\nabla m_l \tag{3.3}$$

$$\rho c_{p,mix}\frac{DT}{Dt} = \nabla \cdot (\lambda + \lambda_t)\nabla T - \nabla \cdot q_{rad} +$$
$$\nabla \cdot \sum_l \rho h_l(T)(D + D_t)\nabla m_l - \rho \sum_l \frac{Dm_l}{Dt}h_l(T) \quad (3.4)$$

$$\frac{\partial \rho m_l}{\partial t} + \nabla \cdot \rho U m_l = \nabla \cdot (D + D_t)\rho \nabla m_l - R_l. \quad (3.5)$$

$$\frac{\partial \rho k}{\partial t} + \nabla \cdot \rho U k = \nabla \cdot \left(\frac{\mu_t}{\sigma_k} + \mu\right)\nabla k - \left(R_{ij}\frac{\partial U_i}{\partial x_j} + \frac{\mu_t}{\rho^2}\nabla\rho \cdot \nabla p\right) - \rho\epsilon \quad (3.6)$$

$$\frac{\partial \rho \epsilon}{\partial t} + \nabla \cdot \rho U \epsilon = \nabla \cdot \left(\frac{\mu_t}{\sigma_\epsilon} + \mu\right)\nabla\epsilon - C_1\frac{\epsilon}{k}\left(R_{ij}\frac{\partial U_i}{\partial x_j} + \frac{\mu_t}{\rho^2}\nabla\rho \cdot \nabla p\right) - C_2\rho\frac{\epsilon^2}{k} \quad (3.7)$$

The stress tensor τ is given by $\tau = \tau_{lam} - R$, where

$$\tau_{lam_{ij}} = \mu\left(\frac{\partial U_i}{\partial x_j} + \frac{\partial U_j}{\partial x_i} - \frac{2}{3}\delta_{ij}\nabla \cdot U\right), \text{ and}$$

$$-R_{ij} = \mu_t\left(\frac{\partial U_i}{\partial x_j} + \frac{\partial U_j}{\partial x_i} - \frac{2}{3}\delta_{ij}\nabla \cdot U\right) - \frac{2}{3}\delta_{ij}\rho k.$$

The turbulent viscosity, thermal conductivity, and mass diffusivity are defined by

$$\mu_t = C_\mu \rho k^2/\epsilon, \quad \lambda_t = c_{p,mix}\mu_t/\sigma_t, \quad D_t = \mu_t/(\rho\sigma_t).$$

Standard values of the turbulence model constants [16] are used: $C_\mu = .09$, $C_1 = 1.44$, $C_2 = 1.92$, $\sigma_k = 1.0$, $\sigma_\epsilon = 1.3$, $\sigma_t = .7$.

The enthalpy h is defined by

$$h = \sum_l m_l h_l(T), \quad (3.8)$$

while the specific heat of the gas mixture, $c_{p,mix}$, is $\sum_l m_l c_{p,l}(T)$. $c_{p,l}(T)$ and $h_l(T)$ are found using GRI-Mech thermochemical data [13]. $h_l(T)$ includes the heat-of-formation of species l. Numerically, equation (3.8) is used only to define the initial and inlet values of h; otherwise, h is found as the solution of (3.3). Moreover, equations (3.3) and (3.4) are redundant. In our numerical method, equation (3.4) is used solely to define intermediate values of T; otherwise, T is computed using h, m_l, and (3.8).

Equations (3.1) and (3.5) are also redundant, as are the trio of equations (3.8), (3.1), and (2.2). These redundancies are accounted for numerically.

The divergence of the radiative heat flux q_{rad} is found using a discrete ordinates model. The discrete ordinates model [9, 22] defines $\nabla \cdot q_{rad}$ by

$$\nabla \cdot q_{rad} = 4k_a\sigma T^4 - k_a\sum_{p,q}w_{p,q}I_{p,q}, \quad (3.9)$$
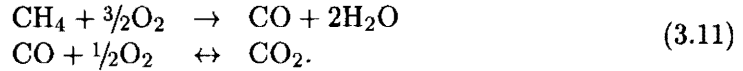
where the subscript p identifies a level of ordinate directions with a particular value of ξ and q indexes the separate ordinates sharing that level. $I_{p,q}$ denotes a radiant

intensity, $w_{p,q}$ an ordinate weight, and k_a the absorption coefficient. In the absence of scattering $I_{p,q}$ satisfies

$$\frac{\mu_{p,q}}{r}\frac{\partial(rI_{p,q})}{\partial r} + \xi_p\frac{\partial I_{p,q}}{\partial z} - \frac{1}{r}\frac{\partial(\eta I)}{\partial \omega} + k_a I_{p,q} = k_a\frac{\sigma T^4}{\pi} \qquad (3.10)$$

where $\sum_{p,q} w_{p,q} = 4\pi$ and μ, ξ, and η denote direction cosines.

In equation (3.5), R_l represents the mass rate of consumption of species l. For the calculations shown in this paper, the following two-step reaction model for methane oxidation [30] is used:

$$\begin{array}{rcl} CH_4 + \frac{3}{2}O_2 & \rightarrow & CO + 2H_2O \\ CO + \frac{1}{2}O_2 & \leftrightarrow & CO_2. \end{array} \qquad (3.11)$$

The corresponding rate of each reaction is the smaller of two rates, the first given by the Arrhenius rate equation recommended in [30] and the second by an eddy-dissipation model [6], respectively. We model the composition of the the fluid with the five species in (3.11) and N_2. Mechanisms that are more complicated than (3.11) can be used with no additional difficulty aside from computational expense.

We now discuss boundary conditions for the governing equations. The inlet profiles of u, v, w, T, h, and m_l have prescribed values. We use recommended [21, 28] inlet values for k and ϵ. At the outflow boundary, the gradients of all quantities are set to zero. At solid walls, the velocity and the gradients of ρ, m_l and k are set to zero. The temperature is a prescribed value. We also use the "law-of-the-wall" [21, 28] to compute ϵ, τ, and the conductive heat flux at the wall. The boundary conditions used in computing $\nabla \cdot q_{rad}$ are model-dependent. For the discrete ordinates model, we use the recommendations in [22].

4   Numerical Algorithm

The algorithm used in advancing the solution from time t^n to $t^n + \Delta t = t^{n+1}$ follows the approach used in [25]. We assume a uniform grid of rectangular cells with widths Δr and Δz indexed by i and j. The center of cell ij is $(i\Delta r, j\Delta z)$. The index ij is used to denote a value centered in cell ij or, equivalently, an average value over the cell. The indices $(i + \frac{1}{2}, j)$, $(i, j + \frac{1}{2})$, and $(i + \frac{1}{2}, j + \frac{1}{2})$ are used to denote values at the right cell edge, the top cell edge, and the top, right corner or node, respectively, of cell ij. At the beginning of the time step, the numerical solution, except for pressure, represents the flow at time t^n at cell centers. The solution for pressure, $\pi_{i+\frac{1}{2},j+\frac{1}{2}}^{n-\frac{1}{2}}$, represents the pressure at the previous half-time step, $t^{n-\frac{1}{2}}$, on cell corners.

The furnace wall-fluid interface is essentially represented by volume and area fractions (Figure 1). The volume fraction Λ_{ij} is the fraction of the volume of cell ij that contains fluid. The area fraction a is the fraction of the area of a cell face in contact with fluid. We denote cells for which $\Lambda_{ij} = 1$ and $a = 1$ on all four edges as "fluid" cells, those for which $\Lambda_{ij} = 0$ as "body" cells, and the remainder as "mixed"

5

cells. The numerical solution is defined on all fluid and mixed cells. Due to the finite element formulation of the projection, the pressure solution is defined on all four nodes of any cell for which $\Lambda_{ij} > 0$.
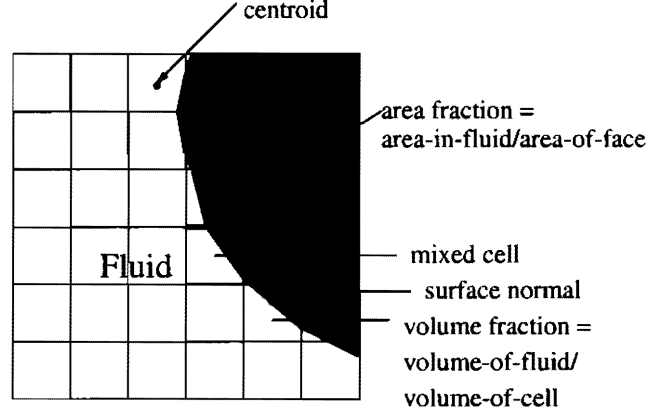

Figure 1: Embedded boundary representation of geometry in two-dimensional cells. Additional integrated quantities are required by the solution of the elliptic equation used to impose the divergence constraint.

The method is a predictor-corrector scheme. In the predictor step, values of k, ϵ, w, T, h, and m_l are computed at time t^{n+1} using a higher-order upwind method for the convective terms and Crank-Nicholson differencing for the diffusive and the reactive terms. In addition, values of U, denoted by U^* or (u^*, v^*), are computed in this step which do not necessarily satisfy the divergence constraint at t^{n+1}. In the corrector step, the divergence constraint is imposed on the velocity through the solution of an elliptic equation, yielding U^{n+1} and $\pi^{n+\frac{1}{2}}_{i+\frac{1}{2},j+\frac{1}{2}}$, the pressure at $t^{n+\frac{1}{2}} = t^n + \Delta t/2$.

The predictor step of the algorithm itself uses a predictor-corrector formulation and consists of the following steps:

(1) Compute Δt:

$$\Delta t = \sigma \min_{ij:\Lambda_{ij} > 0} \left(\frac{\Delta r}{u^n_{ij}}, \frac{\Delta z}{v^n_{ij}} \right) \tag{4.1}$$

where the CFL number σ satisfies $\sigma < 1$.

(2) Compute discrete approximations of the convective terms in the governing equations at time $t^n + \Delta t/2$ using the embedded boundary convective differencing

6

techniques in [2, 26]:

$$(\nabla \cdot \rho U \varphi)_{ij}^{n+\frac{1}{2}} \text{ for } \varphi = h, m_l, w, k, \epsilon \text{ and}$$
$$(U \cdot \nabla \varphi)_{ij}^{n+\frac{1}{2}} \text{ for } \varphi = u, v, T.$$

(3) Compute $\rho_{ij}^{n+1} = \rho_{ij}^{n} - \Delta t \sum_l (\nabla \cdot \rho U m_l)_{ij}^{n+\frac{1}{2}}$.

(4) Compute predicted values $\varphi^{n+1,p}$ of the solution at t^{n+1} for all flow quantities φ, $\varphi = k, \epsilon, m_l, T, h, u^*, v^*$, and w using the Crank-Nicholson method.

(5) Compute $(\nabla \cdot q_{rad})^{n+1}$ using the value of T and other quantities found in (4).

(6) Correct the values of all the flow quantities to provide the solution at time t^{n+1} again using Crank-Nicholson differencing.

In steps (4) and (6) the equations for each of the flow quantities k, ϵ, m_l, T, h, (u^*, v^*), and w are solved sequentially so that only linear systems of equations result from the Crank-Nicholson differencing. The linear systems are solved with a multigrid accelerated Gauss-Seidel scheme [7]. T is advanced as well as h solely to avoid the solution of a non-linear difference equation for h. The updates for species and temperature are themselves performed sequentially in two steps, one accounting for convection and diffusion and the other for kinetics, in order to facilitate the use of complex kinetics mechanisms. In the kinetics update, the system of equations $\partial m_l / \partial t = -R_l$ is integrated with an implicit difference scheme. Temperature is then computed using equation (3.8).

In the remainder of this section, we present the above algorithm in more detail. We first discuss the methodology for the case in which the furnace walls are aligned with the grid boundaries, that is, $\Lambda_{ij} = 1$ for all ij. We then discuss the extensions to account for embedded boundaries.

4.1 Numerical divergence constraint

Several steps in the algorithm require evaluation of $\nabla \cdot U$. The numerical form of the divergence constraint (2.3) requires modification due to the sequential approach.

The continuity equation (3.1) and the equation of state (2.2) are redundant equations for the density ρ. Although the evolution equations with (3.1) replaced by (2.2) analytically conserve mass [24], numerical conservation of mass cannot be guaranteed due to the sequential approach used in the predictor step [29]. We therefore use (3.1) instead of (2.2).

Using (3.1), however, makes it necessary to add an extra term to the discrete form of the divergence constraint (2.3) which accounts for the discrepancy between the values of ρ found by continuity and those found using the equation of state. The divergence constraint (2.3) is incremented as follows:

$$(\nabla \cdot U)_{ij} := (\nabla \cdot U)_{ij} + f\,(\tilde{p}_{ij} - p_{amb})\,\frac{c_{p,mix,ij} - R_{mix,ij}}{\Delta t c_{p,mix,ij}\tilde{p}_{ij}} \equiv \tilde{S}_{ij}, \qquad (4.2)$$

7

where $\tilde{p}_{ij} = R_{mix,ij}\rho_{ij}T_{ij}$ and f is a constant satisfying $f < 1.0$. The extra term in the numerical divergence constraint is found by approximating Dp/Dt in the enthalpy equation for non-isobaric flow [19] by $(\tilde{p}_{ij} - p_{amb})/\Delta t$, rewriting the resultant equation in terms of T, and using (2.3). The term $f(\tilde{p}_{ij} - p_{amb})/\Delta t$ acts to drive the solution back to the constraint $\tilde{p}_{ij} = p_{amb}$. Similar treatments have been used in numerical petroleum reservoir simulation [29].

4.2 Predictor

4.2.1 Computation of convective derivatives

The approximation of the convective derivatives consists of the following steps:

(1) Compute values of $u_{i+\frac{1}{2},j}^{n+\frac{1}{2}}, v_{i+\frac{1}{2},j}^{n+\frac{1}{2}}$ and $u_{i,j+\frac{1}{2}}^{n+\frac{1}{2}}, v_{i,j+\frac{1}{2}}^{n+\frac{1}{2}}$ on all r- and z- cell edges, respectively, using a higher-order upwind scheme [4].

(2) Project edge velocities found in (1) so that they satisfy the divergence constraint.

(3) Recompute $u_{i+\frac{1}{2},j}^{n+\frac{1}{2}}, v_{i+\frac{1}{2},j}^{n+\frac{1}{2}}$ and $u_{i,j+\frac{1}{2}}^{n+\frac{1}{2}}, v_{i,j+\frac{1}{2}}^{n+\frac{1}{2}}$, and compute $\varphi_{i+\frac{1}{2},j}^{n+\frac{1}{2}}, \varphi_{i,j+\frac{1}{2}}^{n+\frac{1}{2}}$ for $\varphi = \rho w, \rho m_l, T, \rho h, \rho k$, and ρe using the higher-order upwind scheme.

(4) Form discrete approximations of convective terms: $(\nabla \cdot (U\varphi))_{ij}^{n+\frac{1}{2}}$, for $\varphi = \rho w, \rho m_l, \rho h, \rho k$, and ρe and $(U \cdot \nabla\varphi)_{ij}^{n+\frac{1}{2}}$ for $\varphi = u, v$, and T.

The first step follows the approach in [4]. First, time-centered left and right edge states, $U_{i+\frac{1}{2},j,L}^{n+\frac{1}{2}}$ and $U_{i+\frac{1}{2},j,R}^{n+\frac{1}{2}}$, at all r-cell faces and bottom and top edge states, $U_{i,j+\frac{1}{2},B}^{n+\frac{1}{2}}$ and $U_{i,j+\frac{1}{2},T}^{n+\frac{1}{2}}$, at all z-cell faces are found with truncated Taylor's series expansions that use monotonicity-limited approximations to the spatial derivatives. The time-centered edge states $U_{i+\frac{1}{2},j}^{n+\frac{1}{2}}$ at all r-cell faces and $U_{i,j+\frac{1}{2}}^{n+\frac{1}{2}}$ at all z-cell faces are then found by an upwinding procedure.

In step (2), we use a MAC projection [15, 4] to enforce the divergence constraint (4.2). The equation

$$\left(D^{MAC}\frac{1}{\rho^n}G^{MAC}\phi\right)_{ij} = \left(D^{MAC}U^{n+\frac{1}{2}}\right)_{ij} - \tilde{S}_{ij}^n \qquad (4.3)$$

is solved for ϕ, where $\tilde{S}^n$ is given by (4.2), and D^{MAC} and G^{MAC} are standard discretizations of the divergence and gradient operators on a staggered grid. The edge velocities are then corrected by

$$\begin{aligned}
u_{i+\frac{1}{2},j}^{n+\frac{1}{2}} &:= u_{i+\frac{1}{2},j}^{n+\frac{1}{2}} - \frac{1}{\rho_{i+\frac{1}{2},j}^n}(G^{MAC}\phi)_{i+\frac{1}{2},j}^r \\
v_{i,j+\frac{1}{2}}^{n+\frac{1}{2}} &:= v_{i,j+\frac{1}{2}}^{n+\frac{1}{2}} - \frac{1}{\rho_{i,j+\frac{1}{2}}^n}(G^{MAC}\phi)_{i,j+\frac{1}{2}}^z.
\end{aligned} \qquad (4.4)$$

In step (3), we recompute $U_{i+\frac{1}{2},j}^{n+\frac{1}{2}}, U_{i,j+\frac{1}{2}}^{n+\frac{1}{2}}$ and compute $\varphi_{i+\frac{1}{2},j}^{n+\frac{1}{2}}, \varphi_{i,j+\frac{1}{2}}^{n+\frac{1}{2}}$ for $\varphi = \rho w, \rho h, \rho m_l, T, \rho k$, and ρe again using the approach in [4] with the modification that the upwind states are found using the MAC-projected edge velocities from step

(2). The discrete approximations to the convective derivatives are then formed using central differences of $\varphi^{n+\frac{1}{2}}_{i+\frac{1}{2},j}$ and $\varphi^{n+\frac{1}{2}}_{i,j+\frac{1}{2}}$.

4.2.2 Crank-Nicholson differencing

In steps (4) and (6) of the predictor we solve difference equations obtained by applying the Crank-Nicholson method to the governing equations. In writing the difference equations below, we use ψ to represent all other flow quantities, including $\nabla \cdot U$. For the following model equation

$$\frac{\partial \rho \varphi}{\partial t} + \nabla \cdot \rho U \varphi = \nabla \cdot \lambda (\varphi, \psi) \nabla \phi + S(\varphi, \psi)$$

the difference scheme has the form

$$\begin{aligned}
\frac{\rho^{n+1}\varphi^{n+1} - \rho^n\varphi^n}{\Delta t} + (\nabla \cdot \rho U \phi)^{n+\frac{1}{2}} &= \tfrac{1}{2}\left(\nabla \cdot \lambda(\varphi^n, \psi^n)\nabla\phi^n + S(\varphi^n, \psi^n)\right. \\
&\quad \left. + \nabla \cdot \lambda\left(\varphi^{n+1,p}, \psi^{n+1,p}\right)\nabla\phi^{n+1} + S\left(\varphi^{n+1,p}, \psi^{n+1,p}\right)\right).
\end{aligned} \quad (4.5)$$

The difference equations for all the quantities except u and v have a similar form. The equations for u and v are coupled and use the gradient of the time-lagged pressure, $(\nabla \pi)^{n-\frac{1}{2}}$. In step (4) of the predictor, $\varphi^{n+1,p}$ and $\psi^{n+1,p}$ are evaluated as φ^n and ψ^n. In step (6), φ^{n+1} and ψ^{n+1} are substituted for $\varphi^{n+1,p}$ and $\psi^{n+1,p}$ as the former become available.

4.2.3 Computation of $\nabla \cdot q_{rad}$

We discretize the discrete ordinate equations as conservation relations for each cell [22] and use diamond-difference formulae with flux-limiting. The temperature field $T^{n+1,p}_{ij}$ is used. The system is solved by successive sweeps through the mesh for each ordinate direction. In the computations for this paper we set both reflection and scattering to zero. The ordinate values are taken from the S_6 set listed in [12].

4.3 Corrector

An approximate projection [3] is now used to enforce the divergence constraint (4.2) and determine $\pi^{n+\frac{1}{2}}$. In the predictor, we use a time-lagged pressure gradient to compute a velocity that does not necessarily satisfy the divergence constraint (4.2),

$$\rho^{n+\frac{1}{2}}_{ij}\frac{U^*_{ij} - U^n_{ij}}{\Delta t} = \frac{1}{2}\left(L^n_{\tau,ij} + L^{n+1}_{\tau,ij}\right) - (U \cdot \nabla U)^{n+\frac{1}{2}}_{ij} - \nabla\pi^{n-\frac{1}{2}}_{ij},$$

where L_τ is the discretization of the first two rows of $\nabla \cdot \tau$. In the projection we enforce

$$\begin{aligned}
\rho^{n+\frac{1}{2}}_{ij}\frac{U^{n+1}_{ij} - U^n_{ij}}{\Delta t} &= \frac{1}{2}\left(L^n_{\tau,ij} + L^{n+1}_{\tau,ij}\right) - (U \cdot \nabla U)^{n+\frac{1}{2}}_{ij} - \nabla\pi^{n+\frac{1}{2}}_{ij} \\
(\nabla \cdot U)^{n+1}_{ij} &= \tilde{S}^{n+1}_{ij}.
\end{aligned}$$

9

From the above, we see that

$$\frac{U_{ij}^{n+1} - U_{ij}^n}{\Delta t} + \frac{1}{\rho_{ij}^{n+\frac{1}{2}}} \left(\nabla\delta\right)_{ij} = \frac{U_{ij}^* - U_{ij}^n}{\Delta t} \tag{4.6}$$

where $\delta_{i+\frac{1}{2},j+\frac{1}{2}} = \pi_{i+\frac{1}{2},j+\frac{1}{2}}^{n+\frac{1}{2}} - \pi_{i+\frac{1}{2},j+\frac{1}{2}}^{n-\frac{1}{2}}$. Taking the divergence of (4.6), we obtain the following equation,

$$\nabla \cdot \left(\frac{1}{\rho_{ij}^{n+\frac{1}{2}}} \left(\nabla\delta\right)_{ij}\right) = \nabla \cdot \left(\frac{U_{ij}^{*,n+1} - U_{ij}^n}{\Delta t}\right) - \frac{\tilde{S}_{ij}^{n+1} - \tilde{S}_{ij}^n}{\Delta t}, \tag{4.7}$$

which we solve using a standard finite-element bilinear discretization. U^{n+1} and $\pi^{n+\frac{1}{2}}$ are then found by

$$\begin{aligned}
U_{ij}^{n+1} &= U_{ij}^* - \frac{\Delta t}{\rho_{ij}^{n+\frac{1}{2}}} \left(\bar{G}\delta\right)_{ij} \\
\pi_{i+\frac{1}{2},j+\frac{1}{2}}^{n+\frac{1}{2}} &= \pi_{i+\frac{1}{2},j+\frac{1}{2}}^{n-\frac{1}{2}} + \delta_{i+\frac{1}{2},j+\frac{1}{2}}
\end{aligned} \tag{4.8}$$

where $\left(\bar{G}\delta\right)_{ij}$ represents the cell average of $\nabla\delta$ over cell ij.

4.4 Extensions for Embedded Boundaries

We now describe how to extend the above methodology to embedded boundaries. The overall philosophy for all steps except the corrector and the computation of $\nabla \cdot \vec{q}_{rad}$ is based on the following strategy for evaluating $\nabla \cdot \vec{F}_{ij}$ in a mixed cell, where $\vec{F} = (F_r, F_z)^T$. First F_r is computed on all r-cell edges for which $a_{i+\frac{1}{2},j} > 0$ and F_z is computed on all z-cell edges for which $a_{i,j+\frac{1}{2}} > 0$. F_r and F_z are computed ignoring the presence of the embedded boundary. In particular, if $\vec{F}$ contains derivative terms, then the discretizations of those derivatives do not account for the boundary. For example, if $\vec{F} = \nabla\phi$, then $F_{r,i+\frac{1}{2},j} = (\phi_{i+1,j} - \phi_{i,j})/\Delta r$. Next the flux $\vec{F}_{wall}$ is computed at the embedded boundary. Diffusive fluxes are evaluated using the "law-of-the-wall", while convective fluxes are set to zero. $\nabla \cdot \vec{F}_{ij}$ is then computed over the fluid portion of the mixed cell using the divergence theorem.

Many of the steps in our methodology involve the solution of a difference equation of the form $L\varphi = f$. Divergence terms enter the algorithm in one of two ways, either in the construction of L or in the evaluation of f. The first case arises, for example, in constructing the left hand side of the difference equations for the MAC projection (4.3) and for the Crank-Nicholson scheme (4.5). The strategy in the preceding paragraph is used to construct L in these situations. The second case arises in computing a divergence used in forming the right side of a difference equation. The approach then is to compute a preliminary value $\nabla \cdot \vec{F}_{ij}^p$ as in the previous paragraph, set $\nabla \cdot \vec{F}_{ij}$ to $\Lambda_{ij}\nabla \cdot \vec{F}_{ij}^p$ in all cells, and redistribute $(1 - \Lambda_{ij})\nabla \cdot \vec{F}_{ij}^p$ in a conservative, volume-weighted manner to the values of $\nabla \cdot \vec{F}_{kl}$ in the cells kl neighboring cell ij.

We use a variation of this last approach to compute convective derivatives [2, 26]. To illustrate, we consider the model equation

$$\frac{\partial \rho \varphi}{\partial t} + \nabla \cdot \rho U \varphi = 0.$$

The strategy is the following. First a reference state $\check{\varphi}$ is constructed in all cells ignoring the embedded boundary. $\check{\varphi}$ is found using the higher upwind method (§4.2.1) with conservative differencing in fluid cells and convective differencing in the mixed cells, i.e.,

$$\frac{\check{\varphi}_{ij} - \varphi_{ij}^n}{\Delta t} = -\left(U \cdot \nabla \varphi\right)_{ij}^{n+\frac{1}{2}},$$

where $(U \cdot \nabla \varphi)_{ij}^{n+\frac{1}{2}}$ is constructed ignoring the embedded boundary. Next, in the mixed cells only, a preliminary value of $(\nabla \cdot \rho U \varphi)_{ij}^{n+\frac{1}{2},p}$ is computed using the approach discussed two paragraphs above, and δM_{ij} is defined by

$$\delta M_{ij} = \left(\varphi_{ij}^n - \check{\varphi}_{ij}\right) - \Delta t \left(\nabla \cdot \rho U \varphi\right)_{ij}^{n+\frac{1}{2},p}.$$

The conservative update for φ is then

$$\varphi_{ij}^{n+1} = \check{\varphi}_{ij} + \delta M_{ij}.$$

This update, however, is potentially unstable for the value of Δt computed in (4.1) due to the presence of small cells. To avoid stability problems, $\check{\varphi}_{ij}^{n+1}$ is instead incremented using a stable but non-conservative update,

$$\check{\varphi}_{ij} := \check{\varphi}_{ij} + \Lambda_{ij} \delta M_{ij}.$$

Conservation is maintained by redistributing $(1 - \Lambda_{ij}) \delta M_{ij}$ in a volume weighted fashion to the values of $\check{\varphi}_{kl}$ in the cells kl adjacent to ij. Finally, the convective derivatives are defined by

$$\left(\nabla \cdot \rho U \varphi\right)_{ij}^{n+\frac{1}{2}} = \left(\varphi_{ij}^n - \check{\varphi}_{ij}\right) / \Delta t.$$

4.4.1 Embedded boundaries: Computation of $\nabla \cdot q_{rad}$

In the presence of embedded boundaries, we model radiative transport effects with a modified S_n discrete ordinate representation. The conservative flux balance on each cell takes the form

$$\frac{\mu_{p,q}}{r_i \Delta r}(r_{i+\frac{1}{2}} a_{i+\frac{1}{2},j} I_{p,q,i+\frac{1}{2},j} - r_{i-\frac{1}{2}} a_{i-\frac{1}{2},j} I_{p,q,i-\frac{1}{2},j}) +$$

$$\frac{\xi_p}{\Delta z}(a_{i,j+\frac{1}{2}} I_{p,q,i,j+\frac{1}{2}} - a_{i,j-\frac{1}{2}} I_{p,q,i,j-\frac{1}{2}}) +$$

$$\frac{\Lambda_{i,j}}{r_i w_{p,q}}(\alpha_{p,q+\frac{1}{2}} I_{p,q+\frac{1}{2},i,j} - \alpha_{p,q-\frac{1}{2}} I_{p,q-\frac{1}{2},i,j}) +$$

$$\frac{\hat{n} \cdot \Omega_{p,q}}{r_i \Delta r \Delta z} r_w L_w I_w + k_a \Lambda_{i,j} I_{p,q,i,j} \quad = \quad \Lambda_{i,j} \frac{\sigma T^4}{\pi},$$

11

where the I_w term represents the flux across a segment of the embedded boundary, r_w is the value of r at the midpoint of the segment, $\hat{n}$ is the normal to the segment, $\Omega_{p,q}$ is an ordinate direction unit vector, L_w is a wall factor, and α is a factor for angular discretization. In fluid cells this reduces to the usual discrete ordinate discretization for axisymmetric coordinates [22]. In order to close the system additional relationships between the center and edge intensities are required. We use a modified form of the diamond-difference relations for this purpose, which for positive μ and ξ is

$$
\begin{aligned}
I_{m,i+\frac{1}{2},j} &= I_{m,i,j} + a_{i-\frac{1}{2},j}(I_{m,i,j} - I_{m,i-\frac{1}{2},j}) \\
I_{m,i,j+\frac{1}{2}} &= I_{m,i,j} + a_{i,j-\frac{1}{2}}(I_{m,i,j} - I_{m,i,j-\frac{1}{2}}).
\end{aligned}
$$

Uniform isotropic flow yields an equation for the wall factor:

$$
\frac{\mu_{p,q}}{r_i \Delta r}(r_{i+\frac{1}{2}} a_{i+\frac{1}{2},j} - r_{i-\frac{1}{2}} a_{i-\frac{1}{2},j}) + \frac{\xi_p}{\Delta z}(a_{i,j+\frac{1}{2}} - a_{i,j-\frac{1}{2}}) +
$$

$$
\frac{\Lambda_{i,j}}{r_i w_{p,q}}(\alpha_{p,q+\frac{1}{2}} - \alpha_{p,q-\frac{1}{2}}) + \frac{\hat{n} \cdot \Omega_{p,q}}{r_i \Delta r \Delta z} r_w L_w = 0.
$$

$\nabla \cdot q_{rad}$ is computed using (3.9) as before.

4.4.2 Embedded boundaries: Corrector

The approximate projection (§4.3) handles the presence of embedded boundaries using a natural extension of the finite-element based discretization discussed above [3] to irregular regions [2]. The basic approach utilizes the same discretization used by Young et al. [31] for full potential transonic flow. We now summarize this approach; see [2] for full details. We rewrite (4.7) as follows:

$$
\nabla \cdot \frac{1}{\rho} \nabla \delta = \nabla \cdot \frac{\partial U^*}{\partial t} - \frac{\partial S}{\partial t}. \tag{4.9}
$$

ρ, $\partial U^*/\partial t$ and $\partial S/\partial t$ are considered to be piecewise constant over each computational cell with values given by (4.6), while δ is considered to be a continuous, piecewise bilinear function. δ can then be expressed as

$$
\delta = \sum_{i+\frac{1}{2},j+\frac{1}{2}} \delta_{i+\frac{1}{2},j+\frac{1}{2}} \chi_{i+\frac{1}{2},j+\frac{1}{2}},
$$

where each function $\chi_{i+\frac{1}{2},j+\frac{1}{2}}$ is a continuous piecewise bilinear function equal to 1 on node $(i + \frac{1}{2}, j + \frac{1}{2})$ and zero on all other nodes. Integrating (4.9) by parts and assuming no flow through the walls, we obtain the following integral equation

$$
\int_\Omega \frac{1}{\rho} \nabla \delta \cdot \nabla \chi_{i+\frac{1}{2},j+\frac{1}{2}} r dr dz = \int_\Omega \frac{\partial U^*}{\partial t} \cdot \nabla \chi_{i+\frac{1}{2},j+\frac{1}{2}} + \frac{\partial S}{\partial t} \chi_{i+\frac{1}{2},j+\frac{1}{2}} \, r dr dz \tag{4.10}
$$

for each node $i + \frac{1}{2}, j + \frac{1}{2}$, where Ω denotes the fluid portion of the computational domain. The left hand side of (4.10) is, in discrete form, a nine-point stencil approximating $\nabla \cdot (1/\rho) \nabla \delta$. The right hand side contains a standard four-point divergence

stencil for $\nabla \cdot (\partial U^*/\partial t)$ and an weighted average of $\partial S/\partial t$ from cell centers to cell nodes. After solving for δ, U and π are updated using (4.8). $(\bar{G}\delta)_{ij}$ in (4.8) is the cell average of $\nabla \delta$ over cell ij. Inflow is accounted for as in [3] by additional terms in the right hand side of (4.10).

5 Computational Results

We now present some results from a calculation using our methodology. We simulate the flow in the Burner Engineering Research Laboratory (BERL) furnace at the Sandia National Laboratory under the conditions reported in [17], specifically, during the testing of a 300 kW IFRF natural gas-fired burner under hot wall conditions in the BERL as part of the GRI SCALING 400 Project. The geometry of the burner is summarized in Figure 2. Air enters the burner at 31.35 m/sec at 312.15° K with a swirl number of .56, while natural gas enters at 22.7 kg/hr at 308.15° K. A more detailed description of the burner geometry as well as the inlet and boundary conditions is provided in [17]. Figure 3 shows some of the computational results at late time. The results compare favorably with the time-steady experimental data. However, the computed maximum temperature is approximately 200° K higher than any reported temperature. This is partially due to the use of a reduced mechanism. The flame also appears to be too narrow near the burner exit, and the central circulation zone exhibits larger negative axial velocities than seen experimentally. We have not yet determined the extent to which these discrepancies are due to the low-Mach number model or other modeling assumptions, or due to the computational methodology. We do not show time-dependent results here, but as in our earlier work [25], the computed state of the furnace reaches approximate steady state at a unreasonably small value of time t. We again believe this is an artifact of the $k - \epsilon$ model.

6 Conclusions and Discussion

We have presented a new methodology for computing unsteady reacting flow in an industrial furnace. Comparisons of late time computational results with time-steady experimental data are so far favorable, but further validation is needed. A better turbulence model is needed to reliably compute time-dependent flow due to the fact that steady state is attained for an unreasonably small value of time t when using the $k - \epsilon$ model. The authors are currently incorporating the methodology presented in this paper into an adaptive mesh refinement scheme [1] to improve computational efficiency.
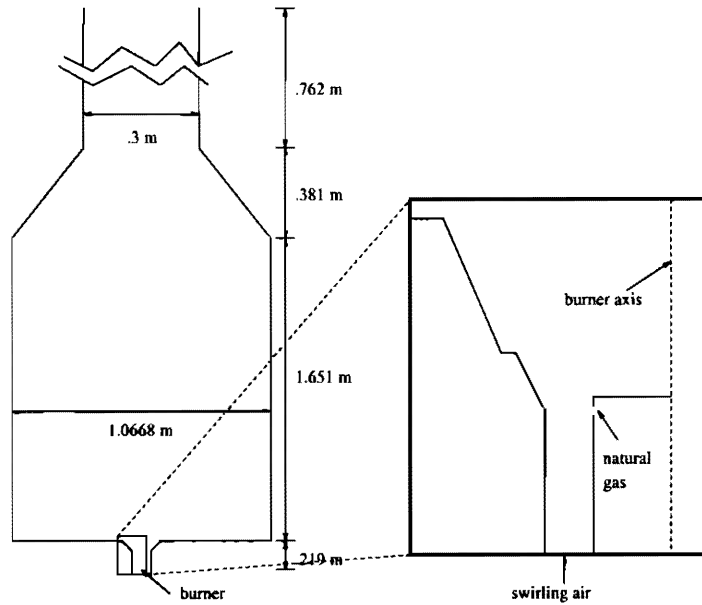
Figure 2: Sketches of the BERL furnace and the IFRF 300kW gas burner.

References

[1] A.S. Almgren, J.B. Bell, P. Colella, and L. H. Howell. An adaptive projection method for the incompressible Euler equations. In *11th AIAA Computational Fluid Dynamics Conference*, Orlando, FL, June 6–9, 1993.

[2] A.S. Almgren, J.B. Bell, P. Colella, and T. Marthaler. Cartesian grid methods for incompressible flow in complex geometries. *SIAM J. Sci. Comput.* (accepted for publication).

[3] A.S. Almgren, J.B. Bell, and W.G. Szymczak. A numerical method for the incompressible Navier-Stokes equations based on an approximate projection. *SIAM J. Sci. Comput.*, accepted for publication. UCRL-JC-112842, Lawrence Livermore National Laboratory, January, 1993.

[4] J. B. Bell, P. Colella, and L. H. Howell. An efficient second-order projection method for viscous incompressible flow. In *10th AIAA Computational Fluid Dynamics Conference*, Honolulu, June 24–27, 1991.

[5] J.B. Bell, P. Colella, and H.M. Glaz. A second-order projection method for the incompressible Navier-Stokes equations. *J. Comput. Phys.*, 85:257–283, 1989.

14

[6] R.W. Bilger. Turbulent diffusion flames. *Ann. Rev. Fluid Mech.*, 21:101–135, 1989.

[7] W.L. Briggs. *A Multigrid Tutorial.* SIAM, Philadelphia, PA, 1987.

[8] L.S. Caretto, A.D. Gosman, S.V. Patankar, and D.B. Spalding. Two calculation procedures for steady, three-dimensional flows with recirculation. In *Proceedings of the Third International Conference on Numerical Methods in Fluid Mechanics.* Paris, France, July, 1972, Vol. II, p.60-68.

[9] B. G. Carlson and K. D. Lathrop. Transport theory—the method of discrete ordinates. In H. Greenspan, C. N. Kelber, and D. Okrent, editors, *Computing Methods in Reactor Physics*, pages 171–266. Gordon and Breach, New York, 1968.

[10] A. Chorin. Numerical solution of the Navier-Stokes equations. *Math. Comp.*, 22:745–762, 1969.

[11] H. Dwyer. Calculation of low Mach number reacting flows. *AIAA Journal*, 28(1):98–105, 1990.

[12] W. A. Fiveland. Discrete-ordinates solutions of the radiative transport equation for rectangular enclosures. *J. Heat Transfer*, 106:699–706, November 1984.

[13] M. Frenklach, H. Wang, C.T. Bowman, R.K. Hanson, G.P. Smith, D.M. Golden, W.C. Gardiner, and V. Lissianski. An optimized kinetics model for for natural gas combustion. 25th International Symposium on Combustion, Irvine, California, 1994, Work-In-Progress PosterSession 3, Number 26.

[14] P.A. Gillis and P.J. Smith. An evaluation of three-dimensional computational combustion and fluid dynamics for industrial furnace geometries. In *Twenty-Third Symposium (International) on Combustion.* pp. 981-991, The Combustion Institute,1990.

[15] F. Harlow and J. Welch. Numerical calculation of time-dependent viscous incompressible flow of fluids with free surfaces. *Phys.Fl.*, 8:2182–2189, 1964.

[16] W.P. Jones and J.H. Whitelaw. Modeling and measurements in turbulent combustion. In *Twentieth Symposium (International) on Combustion.* pp. 233-249, The Combustion Institute,1984.

[17] K.C. Kaufman, W.A. Fiveland, A.A.F. Peters, and R. Weber. The BERL 300kW unstaged natural gas flames with a swirl-stabilized burner. Case 1: Hot-wall conditions. A benchmark problem for validating mathematical combustion models. Technical report. Prepared for the Gas Research Institute under Contract No. 5093-260-2729, November, 1994.

[18] E.E Khalil. *Modeling of Furnaces and Combustors.* Abacus Press, 1982.

[19] K.K. Kuo. *Principles of Combustion*. Wiley-Interscience, New York, 1986.

[20] M. Lai, J.B. Bell, and P. Colella. A projection method for combustion in the zero Mach number limit. In *Proceedings, AIAA 11nd Computational Fluid Dynamics Conference, Orlando, FL.* July 6-9, 1993, p.776-783, AIAA Paper 93-3369-CP.

[21] B.E. Launder and D.B. Spalding. The numerical computation of turbulent flows. *Comp. Meth. Appl. Mech. Eng.*, 3:269–289, 1974.

[22] E. E. Lewis and W. F. Miller, Jr. *Computational Methods of Neutron Transport*. American Nuclear Society, La Grange Park, IL, 1993.

[23] B.F. Magnussen and B.H. Hjertager. On the mathematical modeling of turbulent combustion with special emphasis on soot formation and combustion. In *Sixteenth Symposium (International) on Combustion*. pp. 719-729, The Combustion Institute,1976.

[24] A. Majda and J.A. Sethian. The derivation and numerical solution of the equations for zero Mach number combustion. *Combust. Sci. Tech.*, 42:185–205, 1985.

[25] R.B. Pember, A.S. Almgren, J.B. Bell, P. Colella, L.H. Howell, and M. Lai. A higher-order projection method for the simulation of unsteady turbulent non-premixed combustion in an industrial burner. In *Proceedings of the 8th International Symposium on Transport Phenomena in Combustion*. San Francisco, CA, July 16-20, 1995, also appeared as UCRL-JC-118634, December, 1994.

[26] R.B. Pember, J.B. Bell, P. Colella, W.Y. Crutchfield, and M.L. Welcome. An adaptive Cartesian grid method for unsteady compressible flow in irregular regions. *J. Comput. Phys.*, 120:278–304, 1995.

[27] R.G. Rehm and H.R. Baum. The equations of motion for thermally driven buoyant flows. *N.B.S.J.Res.*, 83:297–308, 1978.

[28] D.G. Sloan, P.J. Smith, and L.D. Smoot. Modeling of swirl in turbulent flow systems. *Prog. Energy Combust. Sci.*, 12:163–250, 1986.

[29] J.A. Trangenstein and J.B. Bell. Mathematical structure of the black-oil model for petroleum reservoir simulation. *SIAM J. Appl. Math.*, 49:749–783, 1989.

[30] C.K. Westbrook and F.L. Dryer. Simplified reaction mechanisms for the oxidation of hydrocarbon fuels in flames. *Combust. Sci. Tech.*, 27:31–43, 1981.

[31] D.P. Young, R.G. Melvin, M.B. Bieterman, F.T. Johnson, S.S. Samant, and J.E. Bussoletti. A locally refined rectangular grid finite element method: Application to computational fluid dynamics and computational physics. *J. Comput. Phys.*, 62:1–66, 1991.

BERL Furnace with IFRF 300kW Gas Burner: Late Time

Temperature	CO mass frac	Radial velocity m/sec

Temperature values: 2211.48071, 1939.55493, 1667.62903, 1395.70325, 1123.77747, 851.85162, 579.92578, 308.00000

CO mass frac values: 0.02199, 0.01884, 0.01570, 0.01256, 0.00942, 0.00628, 0.00314, 0.00000

Radial velocity values: 9.39835, 7.28120, 5.16406, 3.04691, 0.92976, 1.18739, 3.30454, -5.42169

CO2 mass frac	CH4 mass frac	Axial velocity m/sec

CO2 mass frac values: 0.13973, 0.11977, 0.09981, 0.07985, 0.05988, 0.03992, 0.01996, 0.00000

CH4 mass frac values: 0.24532, 0.21028, 0.17523, 0.14018, 0.10514, 0.07009, 0.03505, 0.00000

Axial velocity values: 37.02956, 27.14273, 17.25591, 7.36908, 2.51776, -12.40458, 22.29142, 32.17825
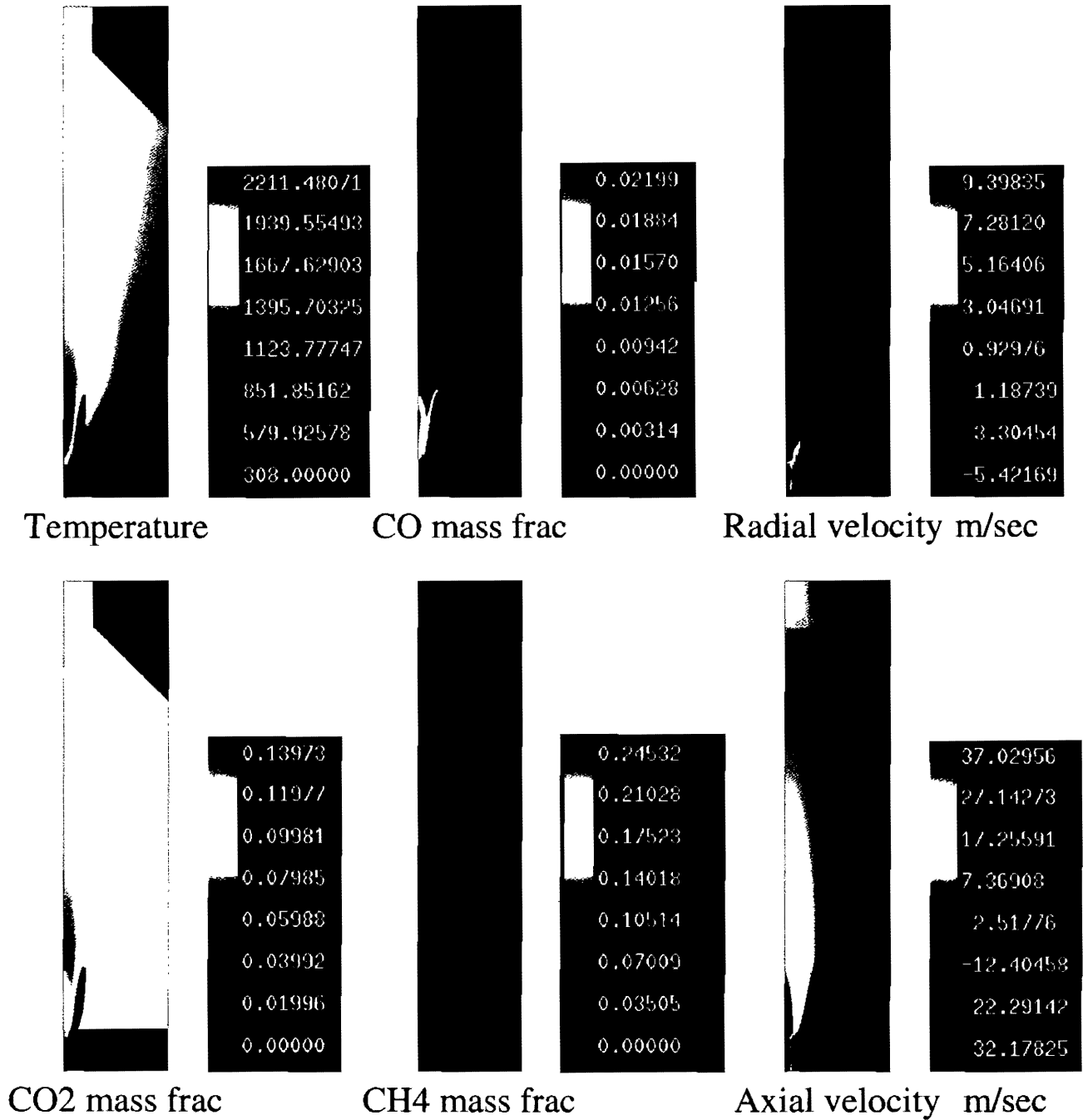
Figure 3: Late time results from a simulation of the BERL furnace under hot wall conditions.